ICAS 2021 SHANGHAI
International Council of the Aeronautical Sciences
32nd Congress of the International Council of the Aeronautical Sciences
September 6-10, 2021
Pudong Shangri-La, Shanghai, China

INVESTIGATION OF AERODYNAMIC INTERACTIONS BETWEEN NACA0012 AIRFOILS IN TANDEM

Muyao Li[1], Hongyi Xu[2]

[1]No.2 High School of East China Normal University, Shanghai, China
[2]Department of Aeronautics and Astronautics, Fudan University, Shanghai, China

Abstract

The aerodynamic interactions are studied between the two NACA0012 airfoils in tandem with each airfoil being pitched at an angle of 4 degree and the Reynolds number being set at 10^4. The studies are based on the solutions of two-dimensional Navier-Stokes equations and the latest vortex identification method using Liutex. The time-averaged aerodynamic coefficient analysis clearly suggests that the rear airfoil gain an obvious aerodynamic advantage over the front airfoil, which provides the evidence to support the phenomenon of bird formation flight. Aside from the mean aerodynamic performance, the detailed interactions between the airfoils are studied in terms of the oscillations in the instantaneous aerodynamic coefficients. The Fourier Transformation is applied to study the spectra of periodically-fluctuating aerodynamic coefficients. Moreover, the oscillating mechanisms in the coefficients are well explained by the vortices identified by Liutex, which are constantly generated at the trailing-edge tips of the both airfoils and are induced by the complex aerodynamic interactions between the airfoils. The front airfoil interacts with the rear one by the vortex shedding from its trailing tip, giving rise to the “vortex pair” corridor that passes around the rear airfoil and induces the vortices on the upper surface of rear airfoil. In addition, the frequency contents are analyzed by the aerodynamic coefficient harmonics. The findings enrich the current understandings of airfoil flows, in particular, the mechanisms of airfoil-vortex interactions.

Keywords: Bird Formation Flight, Airfoil in Tandem, Vortex Identification, Direct Numerical Simulation, Liutex

1. Introduction

Flow past airfoil is well-known a fundamental configuration for aerodynamic research and the aerodynamic interactions between airfoils have long been a focused point of interest to the research community. Although the configuration of airfoils or airfoils in tandem has received many researches for over a long period of time [1,2,3,4,5], most of the numerical investigations were based on the steady Reynolds-averaged Navier-Stokes (RANS) methods with traditional turbulence closure models. However, with the advent of the digital era and the availability of much more powerful computing and data-storage capacities, the direct numerical simulation (DNS) big data are easily accessible to the researchers and therefore, more precise investigations can be conducted based on the more accurate physical model and the more detailed flow physics can be discovered from the study.

Within the context, the current paper conducted the detailed analyses on the DNS data obtained from the database at Aeronautic and Astronautic Department, Fudan University (http://simplefluids.fudan.edu.cn/data), which was aimed at recovering a variety of transient behaviours of flow past airfoil and the aerodynamic interactions between the airfoils in tandem effected by the vortex shedding phenomenon. The current study utilized the latest vortex identification quantity, i.e. Liutex [6], to visualize these transient vortical behaviours and to analyse their consequences to the aerodynamic forces exerting on the airfoils.

The study investigated the transient behaviours of the integrated forces on the airfoils by analysing the frequency contents in the spectra of aerodynamic coefficients, including the lift, pressure and viscous drags. The periodical variations of these coefficients with the time are correlated with the patterns of the vortex shedding on each airfoil, which provides the detailed mechanism of vortex-induced oscillations of the aerodynamic forces exerting on the airfoils. Moreover, the frequency contents found in the FFT analysis are well explained by the vortex travelling behaviours visualized by Liutex and the nonlinearity of the Navier-Stokes equations. The aerodynamic interactions between the airfoils are well understood by finding that the front airfoil constantly generates the vortex shedding from its trailing tip, which gives rise to the 'vortex pair' passageway surrounding the rear airfoil and induce the vortices on the upper surface of rear airfoil. In addition, the rear airfoil aerodynamic advantage over the front airfoil, gained through the vortex interactions, provides an evidence for the phenomenon of bird formation flight. All these findings enrich our current understandings of airfoil flows, in particular, the mechanisms of airfoil-vortex interactions.

2. Mathematical Model, Numerical Methods and Vortex Identification

The DNS data were generated by the governing equations of incompressible unsteady Navier-Stokes equations in two-dimensions. The Reynolds number was set at Re=10^4 and angles of attack at AoA= 4º with the chord of airfoil and the freestream velocity being the characteristic length and velocity, respectively. The equations were solved by the finite-volume space-discretization and the fractional time-step method [7] with the computational domain being set as schematically provided in Figure 1 and the airfoil geometries being implemented into the domain by the immersed boundary method.

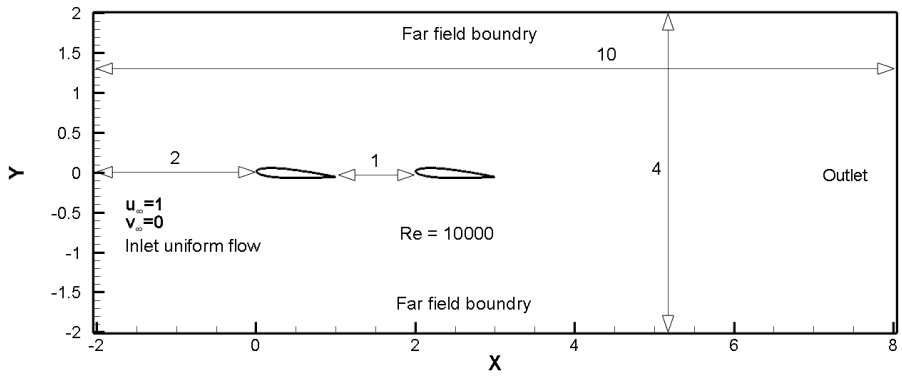

Figure 1 - Schematical drawing of computational domain with the two NACA0012 airfoils placed in tandem with AoA=4º.

The boundary conditions were given in Figure 1 by (1) the inlet uniform flow of $u_\infty = 1$, $v_\infty = 0$; (2) the upper and lower far-field boundary of $\partial u/\partial y$ =0; (3) the downstream outlet condition of $\partial u/\partial x$ =0; and (4) the immersed airfoil wall-boundary of nonslip condition of $u_{wall} = 0$. The initial conditions were set as the uniform velocity field of $u_0 = 1$, $v_0 = 0$.

The DNS flow solver was developed at the Department of Aeronautics and Astronautics, Fudan University, China with both the rigorous numerical and experimental analyses as the verification in Xu [8], and were then further strictly validated by Wang [9,10]. The meshes in the DNS data are given as Nx×Ny = 700*514 and the mesh density is increased toward the airfoil surfaces. The minimum and maximum meshes are $\Delta x_{min} = 0.00151$, $\Delta x_{max} = 0.09036$, $\Delta y_{min} = 0.00195$, $\Delta y_{max} = 0.02836$ in both x and y directions and the time step is equally set at $\Delta t = 2 \times 10^{-4}$. The meshes and the time-step were found being able to provide a stable computation for the entire calculation, and the total number of time steps was 12×10^5. The DNS solutions were converged to the machine accuracy at each time step, which guaranteed the solutions completely satisfies the conservation of mass and momentum.

The vortex identification (VI) was conducted using the third-generation(3rd-G) VI quantity of Liutex and the traditional first-generation(1st-G) VI of vorticity-vector (**ω**) was decomposed into Liutex-vector (**R**) and Shear-vector (**S**) by **ω** = **R** + **S** [6]. The vortex-airfoil interactions were then visualized and investigated by the transient ω_z, R_z, S_z contour distributions, respectively in Figure 2, with the R_z being the most appropriate quantity for representing the vortex motions.

3. Aerodynamic Analyses of Airfoils in Tandem

3.1 Flow Visualizations of Airfoils in Tandem

The flow visualizations are provided in Figure 2, which, for the first time, demonstrates the vortex field of airfoils in tandem and exhibits the difference between the 1st-G VI and the 3rd-G VI as enabled by the ***R-S*** decomposition in the Liutex theory. As can be seen evidently, the 1st -G VI quantity of vorticity (velocity curl) is more correlated with the shearing motions represented by Shear (***S***). Liutex (***R***) as displayed by the contours of |***R***| in Figure 2(c) cleanly identifies the vortex pattern and the cores represented by the Liutex normal maximums and minimums, instead of mixing them in the vorticity as seen in Figure 2(a).

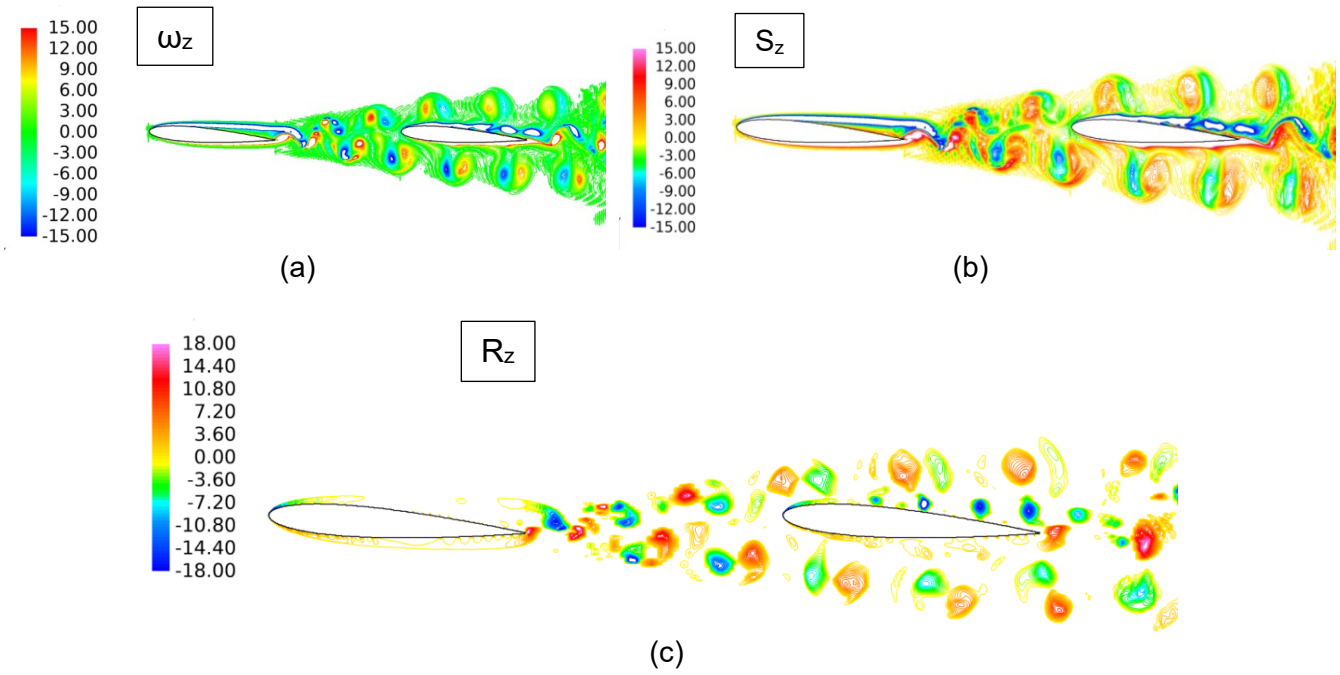

Figure 2 - Fully-developed flow around the airfoils in tandem visualized by (a) Vorticity(|***ω***|= ω_z), (b) Shear(|***S***|=S_z) and (c) Liutex(|***R***|=R_z), with |·| standing for normal operation.

3.2 Study of Airfoil Force Coefficients

Before the analysis, it is necessary to give a definition of the non-dimension lift and drag coefficients (aerodynamic coefficients) involved. The lift, pressure and viscous drag coefficients are generally used to characterize the aerodynamic forces on airfoil [11]. For the coordinate system shown in Figure 1, these coefficients are given as below in the two-dimensional form:

Lift: $$C_{py} = \frac{L_{py}}{0.5\rho {u_\infty}^2 c} = \frac{1}{0.5\rho {u_\infty}^2 c} \oint_\Gamma p n_x dl \quad (1)$$

Pressure drag: $$C_{px} = \frac{D_{px}}{0.5\rho {u_\infty}^2 c} = \frac{1}{0.5\rho {u_\infty}^2 c} \oint_\Gamma p n_y dl \quad (2)$$

Viscous drag: $$C_{vx} = \frac{D_{vx}}{0.5\rho {u_\infty}^2 c} = \frac{1}{0.5\rho {u_\infty}^2 c} \oint_\Gamma \tau_w t_x dl \quad (3)$$

where D_{Px} and L_{Py} represent the resultant forces due to the pressure *p* exerting on the airfoil surface in the x and y directions, respectively, D_{vx} stands for the drag caused by the wall shear stress τ_w on the airfoil surface, n_x and n_y are the x and y components of unit normal vector and t_x is the x components of the unit tangent vector on the airfoil surface, respectively; $\oint_\Gamma ( )\, dl$ is the closed-loop integral around the airfoil and $0.5\rho {u_\infty}^2 c$ is the dimensional scale for these integrals.

Figure 3 presents the aerodynamic coefficients of the front and rear airfoils with the horizontal axis representing the non-dimensional time. The front airfoil is denoted by airfoil-1 with the black curves, while the rear airfoil is represented by airfoil-2 with the red curves. It can be seen from Figure 3 that beyond the time of 16, the flow develops into the statistically stationary state. The black straight-line (airfoil-front-avg) represents the time-averaged coefficients when fully-developed, while the red straight line (airfoil-back-avg) stands for the corresponding mean values of the trailing airfoil.

Comparing the aerodynamic coefficients of the two airfoils in tandem, it is evident that the rear airfoil sitting in the wake of front airfoil presents an evident aerodynamic advantage over the leading one in terms of an increased mean lift by about 13.7%, and the decreased viscous drag by about 19.1% and the pressure drag reduced by 14.7%, respectively. These statistics provide a quantitative and reasonable explanation for the formation flight that most of birds choose to take when migrating for long-distance, since the birds in rear-row of the formation flight can take advantage of the wake generated by the front bird, to obtain an increased lift and reduced drag, and thereby to save the energy consumption in flight [12].

The data from Winslow [1] were used to validate the mean aerodynamic coefficients for the point of Case studies in Figure 3, the current DNS data of NACA0012 airfoil at Re=10^4 with AoA = 4° gives a lift-drag ratio at: (1) 3.540 with the aerodynamically clean leading airfoil and (2) 4.751 with the wake-affected trailing airfoil, which is in quite good consistent with the RANS data obtained by Winslow [1] and demonstrates in the following Figure 3.

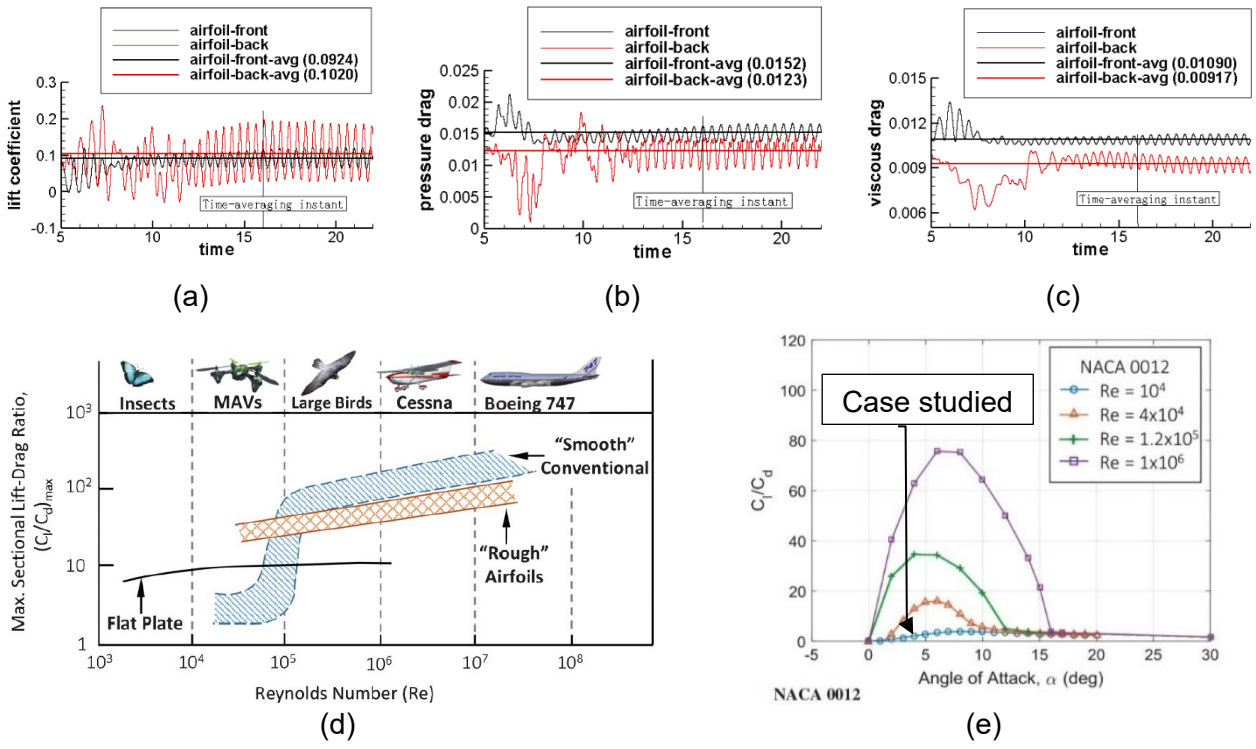

Figure 3 - Time variations of aerodynamic coefficients on the front(black) and rear(red) airfoils: (a) lift, (b) pressure drag, (c) viscous drag coefficients, (d) Range of lift-drag ratios varying with Reynolds numbers for a variety of wings [1], (e) Lift-drag ratio variations with the angles of attack for NACA0012 airfoil at various Reynolds numbers [1]

After analyzing the mean aerodynamic coefficients, the study applied the Fast Fourier Transform (FFT) to study the frequency spectra of these coefficients with the sampling frequency at 34 and the total sampling time-period in 6 from the time instant at 16 to 22. As shown in Figure 4. These spectra all demonstrate a major characteristic harmonic at the frequency of about f0=2.21, or the period at T0=0.4525, for both the front and rear airfoils. The periodic shedding of the vortices from the trailing edge tips of both airfoils is the major source of fluctuations inducing the main frequency of f0=2.21. Moreover, the sub-harmonic with frequency at f1=4.42 (T1=0.2262) is found in the

contents of the spectra for the rear airfoil which well reflects the aerodynamic interactions between the two airfoils. The high-order frequency f2=6.61 is fundamentally generated by the interactions of the two harmonics effected by the nonlinearity in the N-S equation as explained below.

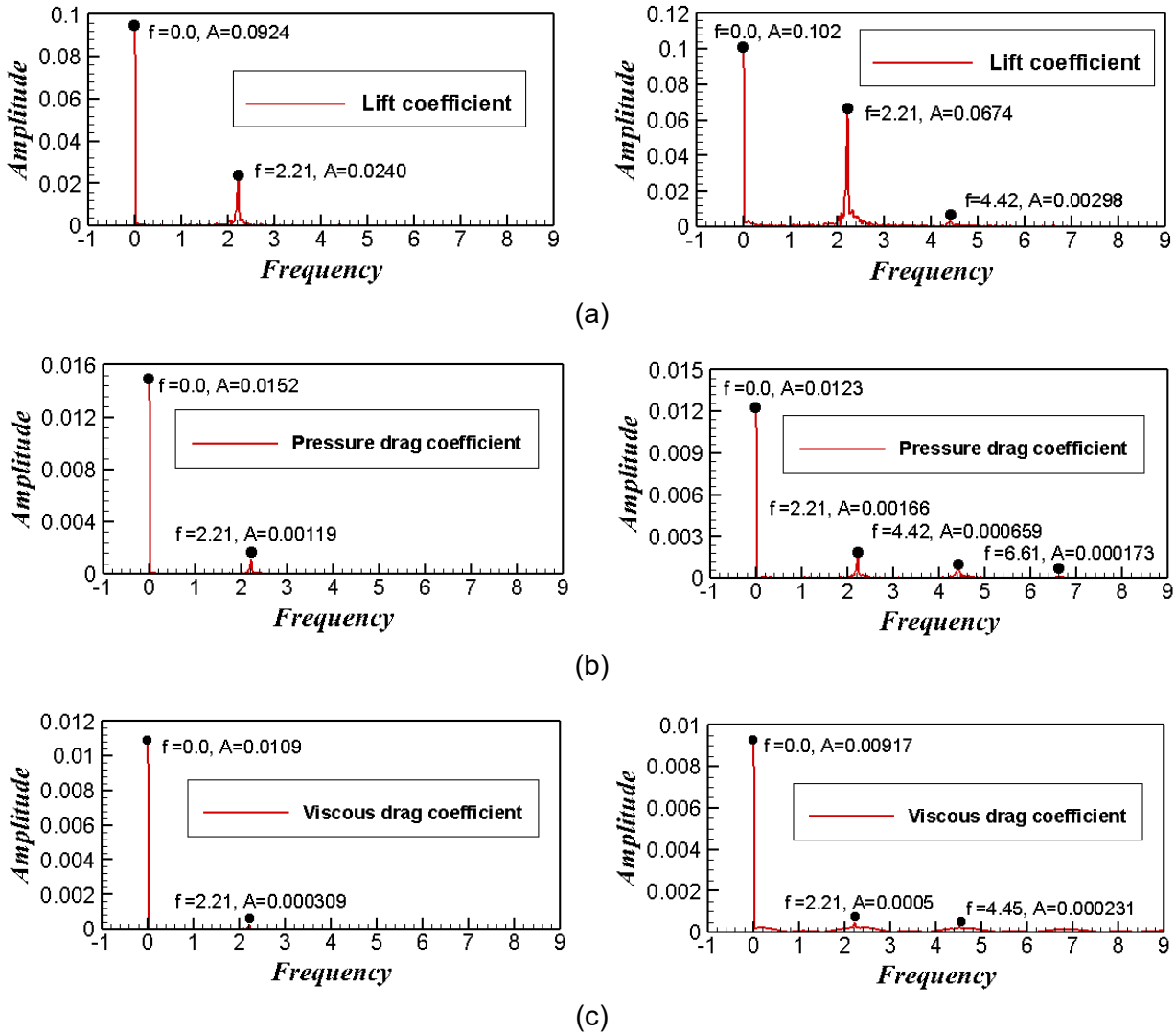

Figure 4 - Spectra of aerodynamic coefficients for the front (left) and rear (right) airfoils: (a) lift (b) pressure drag and (c) viscous drag with **f** and **A** standing for the frequency and amplitude.

3.3 Vortex Characteristics and Airfoil-Vortex Interaction Mechanisms

Based on the 3rd-G VI method of Liutex [6], a variety of vortex generations, identified by the contour distributions of Liutex(|**R**|), and the associated patterns of vortices with their motions are observed around the front and rear airfoils in Figure 5. The current studies investigated the correlations between the harmonics in the coefficient spectra and the vortex motions represented by the Liutex. Thereby, the physical mechanisms of the fluctuations in the various aerodynamic coefficients were well explained and the aerodynamic interactions were profoundly understood in between the front and rear airfoils.

The aerodynamic interferences induced by the leading to the trailing airfoil, as shown in Figure 5, is manifested by a passageway formed by two-line vortex structures on the upper and lower surfaces of the trailing airfoil. The outer vortex row takes the form of "vortex pair" and makes the trailing airfoil located in the "vortex pair" corridor, which induces an inner unidirectionally rotating vortices shedding off at the major frequency aforementioned. As shown in Figures 6 and 7, the vortices of both front and rear airfoils are distinctively shedding off at the same major characteristic frequency of f0=2.21 or period of T0=0.4525.

Thereby, it can be preliminarily concluded that due to the absence of aerodynamic interference, the vortex shedding from the leading airfoil occurs at the trailing edge tip. However, since the trailing airfoil is aerodynamically interfered by the 'vortex-pair' corridor from the leading airfoil, the migration of 'vortex-pair' causes the shear layer near the trailing airfoil's upper surface being broken intermittently (as shown in Figure 2 (b)), which induce the unidirectional vortex around the mid chord of the airfoil. Thereafter, the vortex travels along the upper surface to the trailing-edge tip and leave the airfoil, which may suggest that the vortices on the upper surfaces of both leading and trailing airfoils are the same type since they share with the same shedding-off frequencies.

By analysing the 'vortex pair' impact from the leading airfoil onto the trailing airfoil downstream, the generation mechanism for the sub-harmonic of f1=4.42 or T1=0.2262 in the aerodynamic coefficients can be well understood and clearly explained. While the 'vortex pair' generated by the leading airfoil passes through the leading edge of rear airfoil, the starting time t0 of a cycle is selected as the time instant when the rotation center of the front vortex in the 'vortex pair' coincides with the vertical tangential line of the rear-airfoil leading edge on the upper side, as shown in Figure 8. Then, the time interval can be counted as T1=0.2262 for the next front vortex rotation center in the 'vortex pair' passing the vertical tangential line on the lower side, as shown in the Figure 8, which is identical to the period of the sub-frequency harmonics in the coefficient spectra (see Figure 4). Therefore, it can be concluded that the vortices generated by the leading airfoil periodically influence on the leading edge of the rear airfoil with its aerodynamic impact, which provides the mechanism for the second harmonic in the drag coefficient of rear airfoil.

Finally, the nonlinear form of the terms (uu, uv, vv) in the N-S equations can be used to explain the high-order harmonics in Figure 4. If the system has generated the harmonics of f_0 and f_1, the $\sin(f_0 t) \cdot \cos(f_1 t)$ or $\sin(f_1 t) \cdot \cos(f_0 t)$ components can consequently emerge in the fluid field and then the higher-order harmonics with frequency $(f_0 + f_1)$ can be induced due to the nonlinear interactions, which thereby gives rise to the reason for more harmonics, for instance, the T2=0.1502 or f2=6.61, to occur in the aerodynamic coefficients.

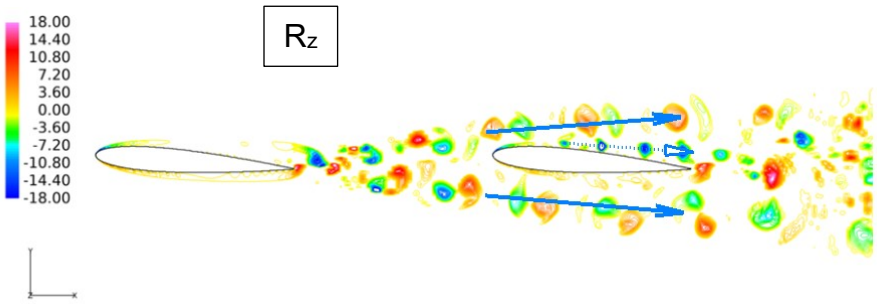

Figure 5 - Instantaneous contour distributions of 3rd-G VI quantity (Liutex normal $|\boldsymbol{R}|=R_z$) with the solid-arrow indicating the upper and lower "vortex pair" corridor and the dotted-arrow denoting the one-way vortex row on the upper surface of rear airfoil.

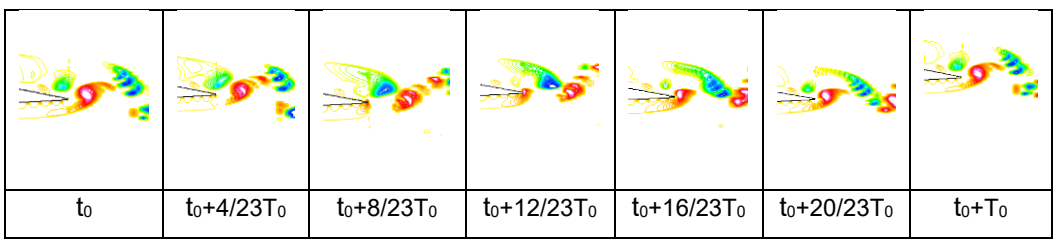

t_0	$t_0+4/23T_0$	$t_0+8/23T_0$	$t_0+12/23T_0$	$t_0+16/23T_0$	$t_0+20/23T_0$	t_0+T_0

Figure 6 - Vortex generation and migration at the trailing edge tip of front airfoil in one period (T_0=0.4525).

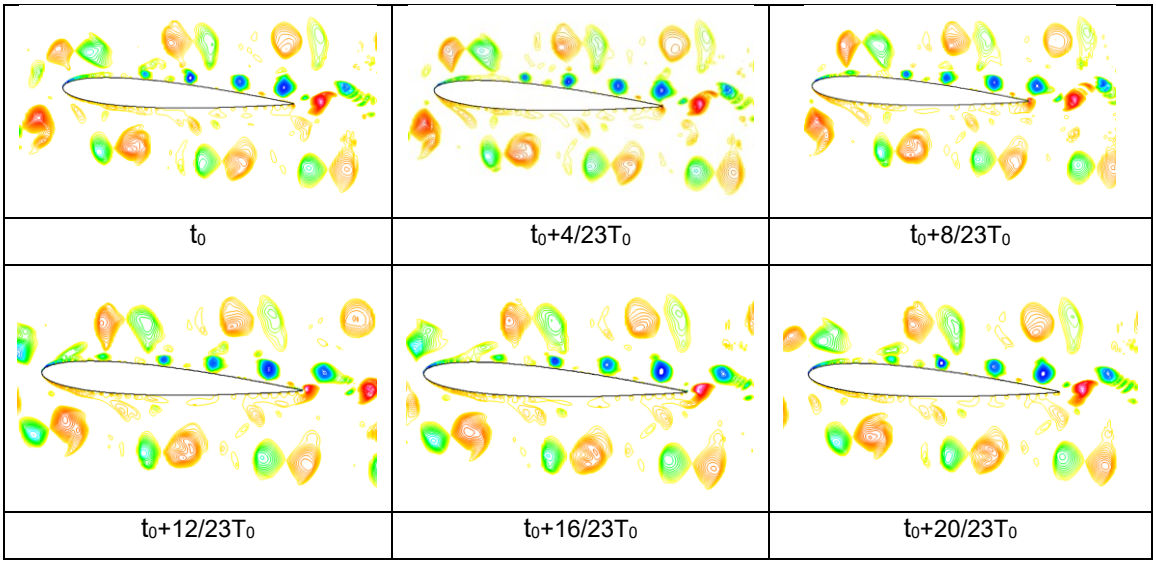

Figure 7 - Vortex generation and migration at the upper and lower surfaces of the rear airfoil and vortices travelling through the leading and trailing edge tips in one period (T_0=0.4525).

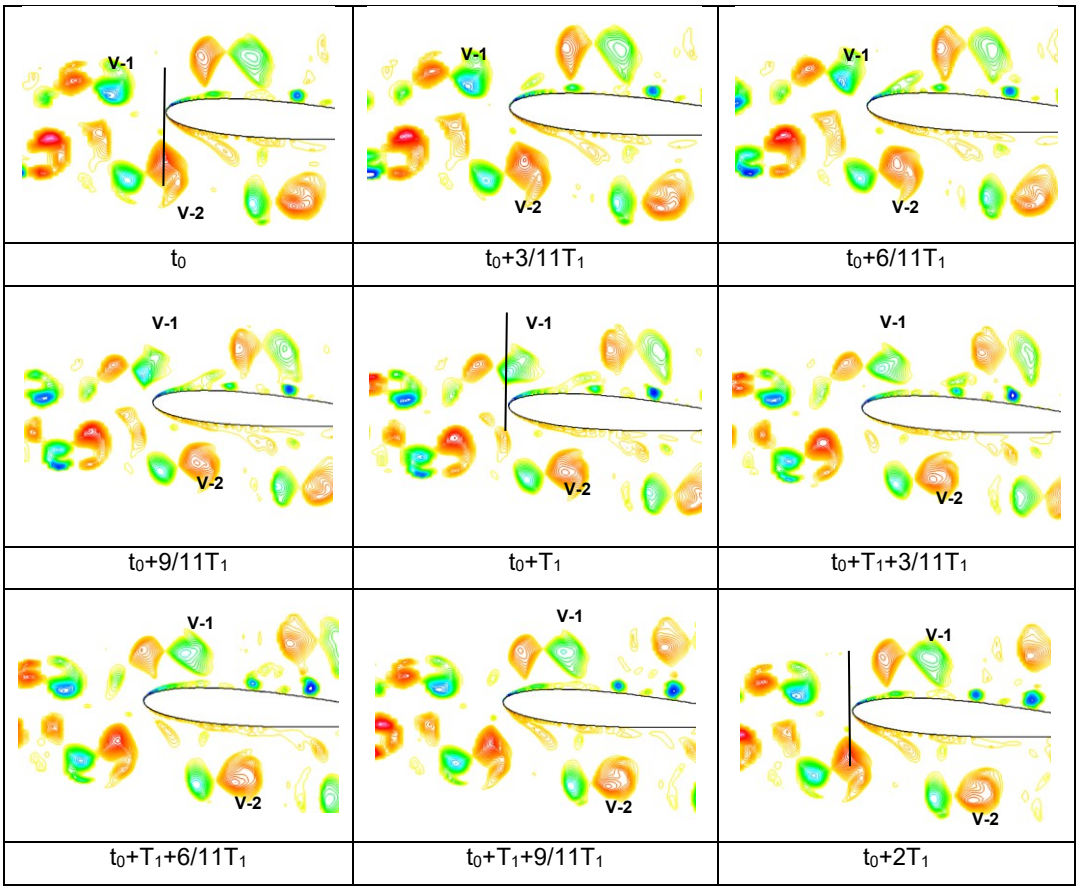

Figure 8 - Front airfoil wake vortices interacting with the leading edge of rear airfoil on the upper and lower sides in a sub-harmonic period of T1=0.2262.

3.4 Physical mechanism of the time variations of aerodynamic coefficients

Figure 9 presents the variation process of the aerodynamic coefficients of the front airfoil in one cycle at five typical moments after the flow develops into the statistically stationary state. The black straight-line (airfoil-front-avg) represents the time-averaged coefficients when fully-developed. It can be seen from Figure 9 that all the aerodynamic coefficients have the same fluctuation cycle time of 0.4525. The lift coefficient and pressure drag coefficient reach the maximal value at the time t=20.09 (A point), while the viscous drag coefficient reaches the minimal value at the same

time. The lift coefficient, pressure drag coefficient and the viscous drag coefficient are all reach the average value at t=20.18 (B point) and t=20.42 (D point). The lift coefficient and pressure drag coefficient reach the minimal value at the time t=20.30 (C point), however the viscous drag coefficient reaches the maximal value at the same moment. At the time t=20.54 (E point), all the aerodynamic coefficients reach the same values as the A point, and then a new cycle starts to repeat.

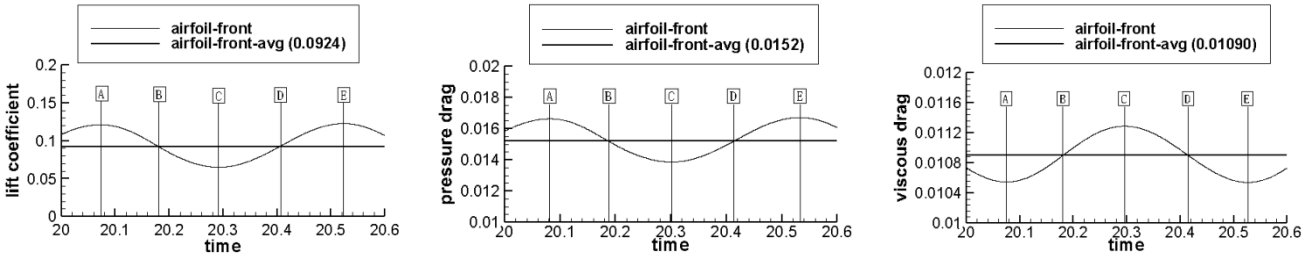

(a) (b) (c)

Figure 9 - The variation process of the aerodynamic coefficients of the front airfoil in one cycle at 5 typical moments A, B, C, D, E corresponding to the (a) lift coefficient; (b) the pressure drag coefficient (c) the coefficient of viscous drag.

The airfoil surface pressure and |**R**| contour distribution of the front airfoil at five typical moments are calculated based the DNS data and presented in the Figure 10. It is observed in Figure 10 (a) and (e) that there are 100% low-pressure zones on the upper surface and 0% low-pressure zone on the lower surface at the A and E moments indicating the maximal lift coefficient, respectively. Figure 10 (b) presents that upper-surface pressure zone reduces to 60%-70% while the lower surface low- pressure zone keeps zero at the B moment, therefore the equivalent lift coefficient reaches the average value. The pressure contour distribution of the D moment shows the 100% low-pressure zone on the upper surface and the 30%-40% low-pressure zone on the lower surface that demonstrates a same pressure difference as the B moment, namely the equivalent lift coefficient reaches the average value. The pressure contour distribution at the C moment presents 60% low- pressure zone on the upper surface and the 80% low-pressure zone on the lower surface that leads to the minimal value of lift. It is concluded that the pressure contour distributions as illustrated at the five typical moments completely match with the variation pattern of the lift coefficient.

The airfoil surface pressure and |**R**| contour distribution of the front airfoil at the five typical moments are provided by Figure 10. During the vortex generation process at the trailing edge tip upper (blue-color vortex), the vortex size increases and the low-pressure zone of upper surface increases accordingly. However, the low-pressure zone of the upper surface shrinks quickly due to the vortex migration or shedding. Similarly, as the vortex size (red-color vortex) increases, the low-pressure zone on lower surface increases accordingly, and the low-pressure zone on the lower surface shrinks quickly in the process of vortex shedding. This correlation between the vortex generation/migration process and the pressure contour distribution variation gives a clear explanation for the fluctuation of the lift coefficient.

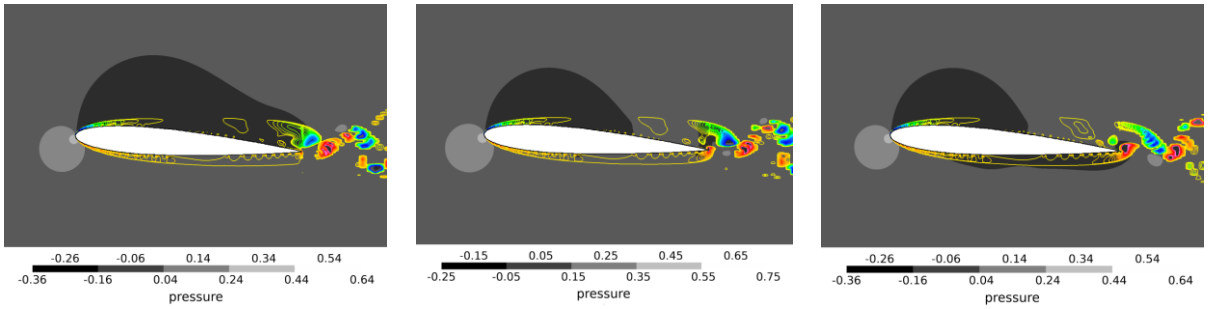

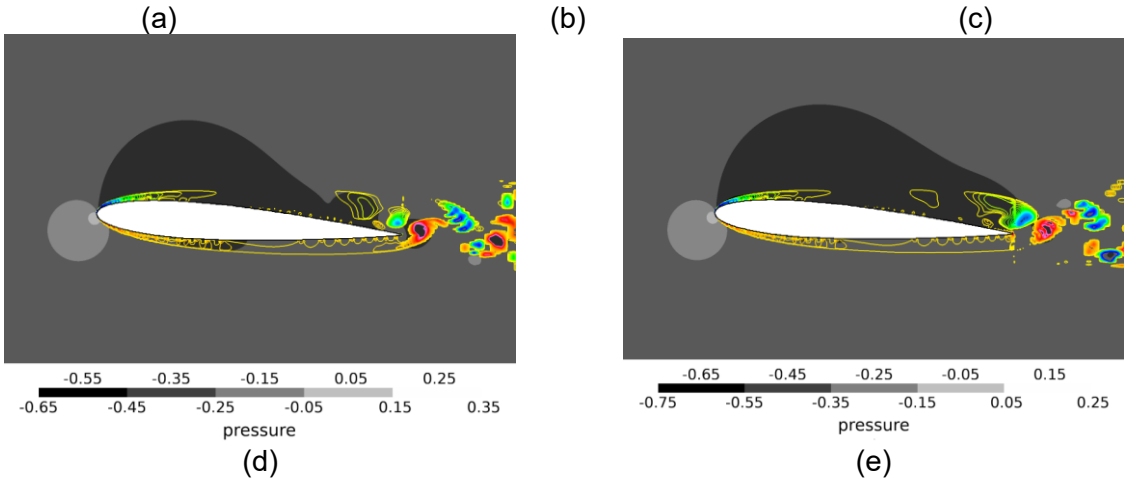

Figure 10 - The airfoil surface pressure and |**R**| contour distribution of the front airfoil at typical moments of (a) A (b) B (c) C (d) D and (e) E.

Figure 11 presents the variation of the aerodynamic coefficients of the rear airfoil in one cycle at typical moments after the flow develops into the statistically stationary state. The red straight-line (airfoil-back-avg) represents the time-averaged coefficients when fully-developed. It can be seen from Figure 11 that all the aerodynamic coefficients also have the same fluctuation cycle at the period of T0=0.4525. The lift coefficient and viscous drag coefficient fluctuate in a sinusoidal waveform while the viscous drag coefficient fluctuate in a rather complex waveform with an apparent sub-harmonics T1=0.2262. As above mentioned, the sub-harmonics in the coefficients are aerodynamically interfered by the 'vortex-pair' corridor from the leading airfoil, in which the sub-harmonic in pressure drag coefficient tends to be bigger. The fluctuation characteristics of the aerodynamic coefficients completely match with the frequency spectra and the corresponding vortex migration processes.

The lift coefficient reaches the average value at the A, C, E moment, while the lift coefficient reaches maximal and minimal values at the B and D moments, respectively, as shown in Figure 11 (a). The airfoil surface pressure and |**R**| contour distribution of the rear airfoil at the five typical moments are calculated based the DNS data and presented in the Figure 12. It is observed in Figure 12 (a) and (e) that there is a 70% low-pressure zone on the upper surface and there is a 10% high-pressure zone on the lower surface at the A and E moments. Figure 12 (c) presents that there is a 60% low- pressure zone on the upper surface while the zero low-pressure zone is found on the lower surface. Therefore, the net lift coefficients at A, C, E moments reach the average value. The pressure contour distribution at the B moment shows the 90% low-pressure zone on the upper surface and the 5% lower-pressure zone on the lower surface, which gives rise to a maximal value. However, the pressure contours at the D moment presents a 60-70% low-pressure zone on the upper surface and a similar percentage of low-pressure zone on the lower surface, which results in a minimal value. The above illustrated pressure contours and their temporal variation match completely with the fluctuation pattern of the lift coefficient on the rear airfoil. Moreover, it can be seen from Figure 12 that the vortex core area (extreme value area identified by |**R**|) is likely accompanied by a local low-pressure zone.

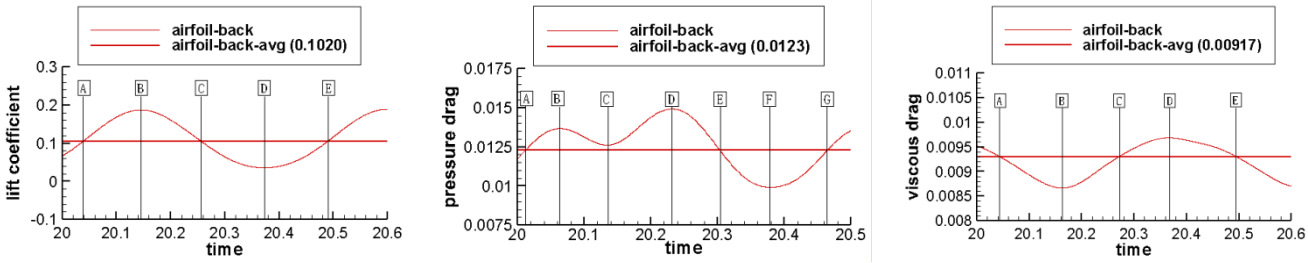

Figure 11 The variations of aerodynamic coefficients on the rear airfoil in one cycle: (a) 5 typical moments A, B, C, D, E corresponding to the lift coefficient; (b) 7 typical moments A, B, C, D, E, F and G corresponding to the pressure drag coefficient; (c) 5 typical moments A, B, C, D, E corresponding to the coefficient of viscous drag.

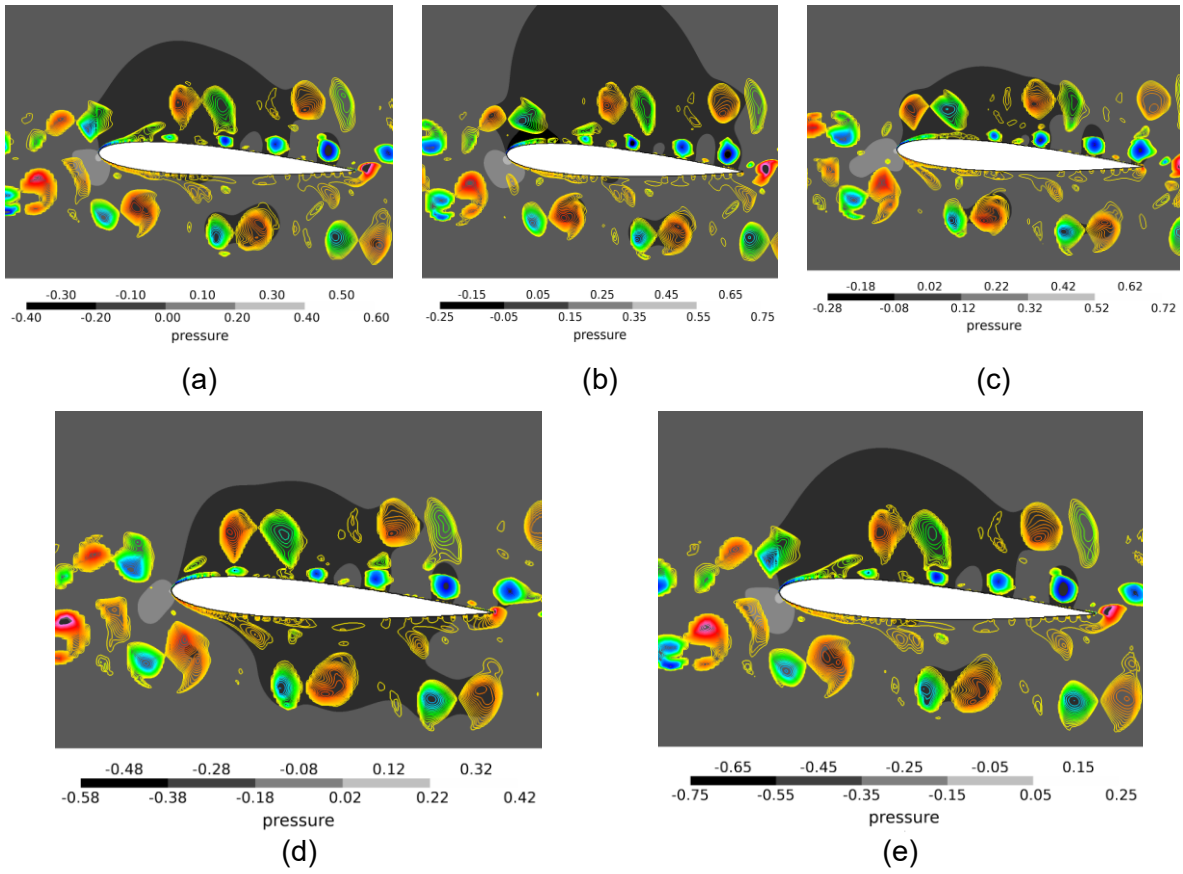

Figure 12 - The airfoil surface pressure and |R| contour distribution of the rear airfoil at typical moments of (a) A (b) B (c) C (d) D and (e) E

4. Conclusions

The 3rd-G VI method is firstly applied to the DNS data of flow with airfoils in tandem to analyse the airfoil-vortex interaction mechanisms. The correlations between the oscillation in aerodynamic coefficients and vortex motion patterns are deeply studied, which provides the in-depth understandings of bird formation flight and airfoil-vortex interactions.

The trailing airfoil gains an apparent aerodynamic advantage by sitting in the wake of a leading airfoil, which provides a quantitative physical explanation for birds to choose the formation flight when migrating long distance. The aerodynamic interactions are concluded to cause an increased lift and a reduced drag, which makes the bird flight more energy efficient.

It is, for the first time, observed through the 3rd-G VI that the leading and trailing airfoils share the same characteristic major frequency in the vortex shedding, which inspire the study of the correlation between the characteristic frequencies and the vortex shedding mechanisms in vortex-airfoil interactions. It is expected to have important impact on understanding the wing turbulence.

Due to the leading airfoil wake, a ‘vortex-pair’ passageway structure is found to play an important role in the aerodynamic interactions with the trailing airfoil. By analysing the characteristics of the vortex patterns and connecting them with non-linearity in the N-S equations, the fundamental generation mechanisms are clarified for the major harmonic and sub-harmonics in the aerodynamic coefficients along with their nonlinear interaction explanations.

The surface pressure and |**R**| contour distribution of the front and rear airfoils are analysed at different typical temporal moments in the fluctuation of the lift coefficient. The results verify that the

pressure contour distribution characteristics are completely matched with the variation pattern of the lift coefficient, which provide an in-depth physical explanation of the lift coefficient fluctuation.

5. Contact Author Email Address

mailto: Hongyi_Xu@fudan.edu.cn

6. Copyright Statement

7. Acknowledgements

The research was funded by the Shanghai Science and Technology Council (No. **20JC1413700**) and by the Shanghai Education Minister (No. **AR960**).

References

[1] Winslow, J., Otsuka, H., Govindarajan, B., & Chopra, I. 2018. Basic Understanding of Airfoil Characteristics at Low Reynolds Numbers (104–105). *Journal of Aircraft*, 55(3), pp1050–1061.

[2] Fanjoy, D., Dorney, D., Fanjoy, D., & Dorney, D. 1997. A study of tandem-airfoil interaction in different flight regimes. *35th Aerospace Sciences Meeting and Exhibit*.

[3] SCHARPF, D. F., & MUELLER, T. J. 1992. Experimental study of a low Reynolds number tandem airfoil configuration. *Journal of Aircraft*, 29(2), pp231–236.

[4] Fanjoy, D. W., & Dorney, D. J. 1996. Numerical Simulations of Tandem-Airfoil Aerodynamics. *SAE Technical Paper Series*.

[5] Zhang Guo-qing, Yang Shu-xing. 2010. Experimental investigation of the aerodynamic characteristics of tandem-airfoil based on low Reynolds number. *Chinese Journal of Computational Mechanics*, 27(4), pp733-737.

[6] Liu, C., Gao, Y., Tian, S., & Dong, X. 2018. Rortex—A new vortex vector definition and vorticity tensor and vector decompositions. *Physics of Fluids*, 30(3), 035103.

[7] Kim, J., & Moin, P. 1985. Application of a fractional-step method to incompressible Navier-Stokes equations. *Journal of Computational Physics*, 59(2), pp308–323.

[8] XU, H. 2009. Direct numerical simulation of turbulence in a square annular duct. *Journal of Fluid Mechanics*, 621, pp23-57.

[9] Wang D., 2020. Direct Numerical Simulations and In-depth Analysis of Fully-developed Thermal Turbulence in Square Annular Duct and Transition Flow around Two Cylinders in Tandem, *PhD Thesis*, Department of Aeronautics and Astronautics, Fudan University.

[10] Wang, D., Li, H., Li, Y., Yu, T., & Xu, H. 2019. Direct numerical simulation and in-depth analysis of thermal turbulence in square annular duct. *International Journal of Heat and Mass Transfer*, 144, 118590.

[11] John D. Anderson. *Fundamentals of Aerodynamics*. 5th edition, McGraw-Hill, ISBN 978-0-07-339810-5.

[12] Weimerskirch H, Martin J, Clerquin Y, et al. 2001. Energy saving in flight formation - Pelicans flying in a 'V' can glide for extended periods using the other birds' air streams. *Nature*, 413(6857): pp 697-698.